Neutrino transition magnetic moment in $U(1)_X$SSM*

Long Ruan (阮龙)[1,2,3] Shu-Min Zhao (赵树民)[1,2,3†] Ming-Yue Liu (刘明月)[1,2,3] Xing-Yu Han (韩星宇)[1,2,3]
Xi Wang (王曦)[1,2,3] Xing-Xing Dong (董幸幸)[1,2,3,4‡]

[1]Department of Physics, Hebei University, Baoding 071002, China
[2]Hebei Key Laboratory of High-precision Computation and Application of Quantum Field Theory, Baoding 071002, China
[3]Hebei Research Center of the Basic Discipline for Computational Physics, Baoding 071002, China
[4]Departamento de Fisica and CFTP, Instituto Superior Técnico, Universidade de Lisboa, Av.Rovisco Pais 1,1049-001 Lisboa, Portugal

Abstract: In this study, we investigated the neutrino transition magnetic moment in $U(1)_X$SSM. $U(1)_X$SSM is the $U(1)$extension of the Minimal Supersymmetric Standard Model (MSSM), and its local gauge group is extended to $SU(3)_C\times SU(2)_L\times U(1)_Y\times U(1)_X$. To obtain this model, three singlet new Higgs superfields and right-handed neutrinos are added to the MSSM, which can explain the results of neutrino oscillation experiments. The neutrino transition magnetic moment is induced by electroweak radiative corrections. By applying the effective Lagrangian method and on-shell scheme, we studied the associated Feynman diagrams and transition magnetic moment of neutrinos in the model. We fit experimental data for neutrino mass variances and mixing angles. Based on the range of data selection, the influences of different sensitive parameters on the results were analyzed. The numerical analysis shows that many parameters, such as g_X, M_2, μ, λ_H, and g_{YX}, have an effect on the neutrino transition magnetic moment. In our numerical results, the order of magnitude of μ_{ij}^M/μ_B is approximately $10^{-20}\sim 10^{-19}$.

Keywords: transition magnetic moment, $U(1)_X$SSM, neutrino

DOI: 10.1088/1674-1137/adc978 **CSTR:** 32044.14.ChinesePhysicsC.49083104

I. INTRODUCTION

The Standard Model (SM) comes under the umbrella of quantum field theory, which describes the three main forces, namely the strong, weak, and electromagnetic forces [1−4]. Moreover, it predicts the existence of the Higgs. Although the SM has been a great success, its flaws are evident. It does not explain the mass problem of neutrinos or the related issue of dark matter and cannot describe gravity [5−7]. Therefore, it must be extended. Scientists have proposed many extensions to the SM, among which the Minimal Supersymmetric Standard Model (MSSM) is a popular one. However, problems exist in the MSSM as well, such as the μ-problem [8] and massless neutrinos [9]. To overcome these problems, we propose applying $U(1)_X$SSM. Using this model, we study the neutrino transition magnetic moment, which may indirectly lead to a new understanding of the neutrino properties and mechanism of neutrino mass generation. In addition, the neutrino transition magnetic moment may be employed to verify the correctness of $U(1)_X$SSM to some extent. It is also important in the long distance propagation of neutrinos within the magnetic fields of matter and vacuum [10]. Previous research on the neutrino transition magnetic moment includes analyses of Majorana neutrino effects on supernova neutrino oscillations [11] and explanations of electron recoil anomalies [12]. However, in this study, we explore this phenomenon within a distinct model, aiming to contribute new findings.

$U(1)_X$SSM is the extension of the MSSM including the $U(1)_X$ gauge group, and the symmetry group is $SU(3)_C\times SU(2)_L\times U(1)_Y\times U(1)_X$ [13]. This extension adds three Higgs singlet superfields and right-handed neutrino superfields to the MSSM. Consequently, there are five neutral CP-even Higgs component fields (H_u^0, H_d^0, ϕ_η^0, $\phi_{\bar{\eta}}^0$, ϕ_S^0) in the model; they mix, forming a 5×5 mass-squared matrix. The mass of the lightest CP-even Higgs particle can be improved at the tree level. In $U(1)_X$SSM,

Received 17 December 2024; Accepted 7 April 2025; Published online 8 April 2025

* Supported by National Natural Science Foundation of China (NNSFC, 12075074), Natural Science Foundation of Hebei Province (A2020201002, A2023201040, A2022201022, A2022201017, A2023201041), Natural Science Foundation of Hebei Education Department (QN2022173), Post-graduate's Innovation Fund Project of Hebei University (HBU2024SS042), Scholarship Council (CSC, 202408130113). X. Dong acknowledges support from Fundação para a Ciência e a Tecnologia (FCT, Portugal) through the projects CFTP FCT Unit UIDB/00777/2020 and UIDP/00777/2020

† E-mail: zhaosm@hbu.edu.cn
‡ E-mail: dongxx@hbu.edu.cn

the small hierarchy problem in the MSSM is alleviated through the added right-handed neutrinos, sneutrinos, and extra Higgs singlets. The μ-problem existing in the MSSM is mitigated after the spontaneous symmetry breaking of the S field in vacuum through $\lambda_H \hat{S}\hat{H}_u\hat{H}_d$. Through the term $Y_\nu \hat{\nu}\hat{l}\hat{H}_u$, the right-handed and left-handed neutrinos mix, which makes light neutrinos to acquire extremely small masses through the seesaw mechanism. The existence of supersymmetry provides a natural candidate for dark matter: neutralino. Meanwhile, $SU(3)_C\times SU(2)_L\times U(1)_Y\times U(1)_X$provides several dark matter candidates such as neutralino and sneutrino (CP-even, CP-odd). Moreover, it protects the Higgs mass from radiative correction by massive particles, which solves the gauge hierarchy. Under $U(1)_X$SSM, the transition magnetic moment of neutrino is induced by electroweak radiative corrections.

Previous studies [10] investigated the neutrino transition magnetic moment using the effective Lagrangian method and mass-shell scheme, yielding reasonable numerical results. In this paper, a more comprehensive study of the neutrino transition magnetic moment within$U(1)_X$SSM is presented. Using the effective Lagrangian method and mass-shell scheme, we obtained an expression for the neutrino transition magnetic moment. We then derived the relevant Feynman diagrams and calculated the neutrino transition moment by combining the operators. Leveraging numerical calculations, we performed neutrino mixing within experimentally constrained parameter ranges to determine viable parameter values. Additionally, we compared the effects of different reasonable parameters on the transition magnetic moment and obtained numerical results.

The paper is organized according to the following structure. In Sec. II, we mainly introduce $U(1)_X$SSM, including its superpotential, general soft breaking terms, mass matrices, and couplings. In Sec. III, we derive the analytical expressions of the transition magnetic moment for the neutrino. In Sec. IV, we present relevant parameters and numerical analysis. In Sec. V, we present a summary of this study. Some formulae are presented in Appendices.

II. ESSENTIAL ASPECTS OF $U(1)_X$SSM

$U(1)_X$SSM is the extension of MSSM in which the local gauge group is $SU(3)_C\times SU(2)_L\times U(1)_Y\times U(1)_X$. $U(1)_X$SSM has new superfields that include three Higgs singlets, $\hat{\eta}$, $\hat{\bar{\eta}}$, $\hat{S}$, and right-handed neutrinos $\hat{\nu}_i$. The corresponding superpotential of $U(1)_X$SSM is expressed as

$$\begin{aligned} W =& l_W\hat{S}+\mu\hat{H}_u\hat{H}_d+M_S\hat{S}\hat{S}-Y_d\hat{d}\hat{q}\hat{H}_d-Y_e\hat{e}\hat{l}\hat{H}_d+\lambda_H\hat{S}\hat{H}_u\hat{H}_d \\ &+\lambda_C\hat{S}\hat{\eta}\hat{\bar{\eta}}+\frac{\kappa}{3}\hat{S}\hat{S}\hat{S}+Y_u\hat{u}\hat{q}\hat{H}_u+Y_X\hat{\nu}\hat{\bar{\eta}}\hat{\nu}+Y_\nu\hat{\nu}\hat{l}\hat{H}_u. \end{aligned} \tag{1}$$

The two Higgs doublets and three Higgs singlets can be expressed as

$$\begin{aligned} H_u =& \begin{pmatrix} H_u^+ \\ \frac{1}{\sqrt{2}}\left(v_u+H_u^0+\mathrm{i}P_u^0\right) \end{pmatrix}, \\ H_d =& \begin{pmatrix} \frac{1}{\sqrt{2}}\left(v_d+H_d^0+\mathrm{i}P_d^0\right) \\ H_d^- \end{pmatrix}, \\ \eta =& \frac{1}{\sqrt{2}}\left(v_\eta+\phi_\eta^0+\mathrm{i}P_\eta^0\right),\quad \bar{\eta}=\frac{1}{\sqrt{2}}\left(v_{\bar{\eta}}+\phi_{\bar{\eta}}^0+\mathrm{i}P_{\bar{\eta}}^0\right), \\ S =& \frac{1}{\sqrt{2}}\left(v_S+\phi_S^0+\mathrm{i}P_S^0\right). \end{aligned} \tag{2}$$

The vacuum expectation values of the states H_u, H_d, η, $\bar{\eta}$, S are respectively v_u, v_d, v_η, $v_{\bar{\eta}}$, and v_S. H_u^+ is the charged part of the doublet H_u. $H_u^0(P_u^0)$ is the neutral CP-even (CP-odd) part of H_u. A similar condition is considered for the doublet H_d. $\phi_\eta^0(P_\eta^0)$ is the CP-even (CP-odd) part of the singlet η. $\phi_{\bar{\eta}}^0(P_{\bar{\eta}}^0)$ is the CP-even (CP-odd) part of the singlet $\bar{\eta}$. $\phi_S^0(P_S^0)$ is the CP-even (CP-odd) part of the singlet S.

There are two angles defined as $\tan\beta=v_u/v_d$ and $\tan\beta_\eta=v_{\bar{\eta}}/v_\eta$. The soft SUSY breaking terms of $U(1)_X$SSM are

$$\begin{aligned} \mathcal{L}_{\text{soft}} =& \mathcal{L}_{\text{soft}}^{\text{MSSM}}-B_S S^2-L_S S-\frac{T_\kappa}{3}S^3-T_{\lambda_C}S\eta\bar{\eta} \\ &+\epsilon_{ij}T_{\lambda_H}S H_d^i H_u^j-T_X^{IJ}\bar{\eta}\tilde{\nu}_R^{*I}\tilde{\nu}_R^{*J}+\epsilon_{ij}T_\nu^{IJ}H_u^i\tilde{\nu}_R^{I*}\tilde{l}_j^J \\ &-m_\eta^2|\eta|^2-m_{\bar{\eta}}^2|\bar{\eta}|^2-m_S^2S^2 \\ &-(m_{\tilde{\nu}_R}^2)^{IJ}\tilde{\nu}_R^{I*}\tilde{\nu}_R^J-\frac{1}{2}\left(M_S\lambda_{\tilde{X}}^2+2M_{BB'}\lambda_{\tilde{B}}\lambda_{\tilde{X}}\right)+\text{h.c}. \end{aligned} \tag{3}$$

$\mathcal{L}_{\text{soft}}^{\text{MSSM}}$ represents the soft breaking terms of the MSSM. $\lambda_{\tilde{B}}$ is the $U(1)_Y$ gaugino, which is the supersymmetric partner of the $U(1)_Y$ gauge boson B^μ. The boson of the added gauge group $U(1)_X$ is X^μ, whose supersymmetric partner is $\lambda_{\tilde{X}}$.

The particle content and charge assignments for $U(1)_X$ SSM are listed in Table 1. In a previous study of ours, we demonstrated that $U(1)_X$SSM is anomaly free [13].

The covariant derivatives of $U(1)_X$SSM can be expressed as

$$D_\mu=\partial_\mu-\mathrm{i}\begin{pmatrix} Y, & X \end{pmatrix}\begin{pmatrix} g_1, & g_{YX} \\ 0, & g_X \end{pmatrix}\begin{pmatrix} A_\mu^Y \\ A_\mu^X \end{pmatrix}. \tag{4}$$

Compared with the MSSM, $U(1)_X$SSM includes a new effect called gauge kinetic mixing produced by Abelian groups $U(1)_Y$ and $U(1)_X$. The basis conversion occurs

Table 1. Superfields in $U(1)_X$SSM.

Superfields	$\hat{q}_i$	$\hat{u}_i^c$	$\hat{d}_i^c$	$\hat{l}_i$	$\hat{e}_i^c$	$\hat{\nu}_i$	$\hat{H}_u$	$\hat{H}_d$	$\hat{\eta}$	$\hat{\bar{\eta}}$	$\hat{S}$
$SU(3)_C$	3	$\bar{3}$	$\bar{3}$	1	1	1	1	1	1	1	1
$SU(2)_L$	2	1	1	2	1	1	2	2	1	1	1
$U(1)_Y$	1/6	−2/3	1/3	−1/2	1	0	1/2	−1/2	0	0	0
$U(1)_X$	0	−1/2	1/2	0	1/2	−1/2	1/2	−1/2	−1	1	0

when the rotation matrix R ($R^TR=1$) is used and is due to the fact that the two Abelian gauge groups are uninterrupted. The basis conversion can be described by [14−17]

$$D_\mu=\partial_\mu-\mathrm{i}\begin{pmatrix} Y^Y, & Y^X \end{pmatrix}\begin{pmatrix} g_Y, & g'_{YX} \\ g'_{XY}, & g'_X \end{pmatrix}R^TR\begin{pmatrix} A'^Y_\mu \\ A'^X_\mu \end{pmatrix} \tag{5}$$

where A'^Y_μ and A'^X_μ respectively represent the gauge fields of $U(1)_Y$ and $U(1)_X$. Equation (5) can be reduced to [14, 16, 17]

$$\begin{pmatrix} g_Y, & g'_{YX} \\ g'_{XY}, & g'_X \end{pmatrix}R^T=\begin{pmatrix} g_1, & g_{YX} \\ 0, & g_X \end{pmatrix},$$
$$R\begin{pmatrix} A'^Y_\mu \\ A'^X_\mu \end{pmatrix}=\begin{pmatrix} A^Y_\mu \\ A^X_\mu \end{pmatrix}. \tag{6}$$

Here, g_X expresses the gauge coupling constant of the $U(1)_X$ group and g_{YX} expresses the mixing gauge coupling constant of the $U(1)_X$ and $U(1)_Y$ groups.

Some useful mass matrices and required couplings in this model can be found in Appendix A.

III. FORMULATION

The magnetic dipole moment (MDM) and electric dipole moment (EDM) of the neutrino can be expressed as the following operators:

$$\mathcal{L}_{\rm MDM}=\frac{1}{2}\mu_{ij}\bar{\psi}_i\sigma^{\mu\nu}\psi_jF_{\mu\nu},$$
$$\mathcal{L}_{\rm EDM}=\frac{\mathrm{i}}{2}\epsilon_{ij}\bar{\psi}_i\sigma^{\mu\nu}\gamma_5\psi_jF_{\mu\nu}, \tag{7}$$

where $F_{\mu\nu}$ is the electromagnetic field strength, $\sigma^{\mu\nu}=\frac{\mathrm{i}}{2}[\gamma^\mu,\gamma^\nu]$, $\psi_{i,j}$denotes the four-component Dirac fermions, andμ_{ij} and ϵ_{ij} are the Dirac diagonal ($i=j$) or transition ($i\neq j$) MDM and EDM between states ψ_i and ψ_j, respectively.

Given that $\not{p}=m_f\ll m_V$ for on-shell fermions and $\not{k}\to 0\ll m_V$ for photons, we can conveniently obtain the contribution of the loop diagram to the fermionic diagonal MDM and EDM using the effective Lagrangian method. Then, we can expand the amplitude of corresponding triangle diagrams based on the external momenta of fermions and photons. After matching the effective theory with the holonomic theory, we can obtain all high-dimension operators along with their coefficients. We only need to keep the following six dimension operators for subsequent calculations:

$$\begin{aligned}
O_1^{L,R}&=e\bar{\psi}_i(i\mathcal{D})^3P_{L,R}\psi_j,\\
O_2^{L,R}&=e\overline{(i\mathcal{D}_\mu\psi_i)}\gamma^\mu F\cdot\sigma P_{L,R}\psi_j,\\
O_3^{L,R}&=e\bar{\psi}_iF\cdot\sigma\gamma^\mu P_{L,R}(i\mathcal{D}_\mu\psi_j),\\
O_4^{L,R}&=e\bar{\psi}_i(\partial^\mu F_{\mu\nu})\gamma^\nu P_{L,R}\psi_j,\\
O_5^{L,R}&=em_{\psi_i}\bar{\psi}_i(i\mathcal{D})^2P_{L,R}\psi_j,\\
O_6^{L,R}&=em_{\psi_i}\bar{\psi}_iF\cdot\sigma P_{L,R}\psi_j,
\end{aligned} \tag{8}$$

where $P_L=\frac{1}{2}(1-\gamma_5)$, $P_R=\frac{1}{2}(1+\gamma_5)$, $\mathcal{D}_\mu=\partial^\mu+\mathrm{i}eA_\mu$, and m_{ψ_i} is the mass of fermion ψ_i. The effective vertices with one external photon are expressed as

$$\begin{aligned}
O_1^{L,R}&=\mathrm{i}e\{[(p+k)^2+p^2]\gamma_\rho+(\not{p}+\not{k})\gamma_\rho\not{p}\}P_{L,R},\\
O_2^{L,R}&=\mathrm{i}e(\not{p}+\not{k})[\not{k},\gamma_\rho]P_{L,R},\\
O_3^{L,R}&=\mathrm{i}e[\not{k},\gamma_\rho]\not{p}P_{L,R},\\
O_4^{L,R}&=\mathrm{i}e(k^2\gamma_\rho-\not{k}k_\rho)P_{L,R},\\
O_5^{L,R}&=\mathrm{i}em_{\psi_i}\{(\not{p}+\not{k})\gamma_\rho+\gamma_\rho\not{p}\}P_{L,R},\\
O_6^{L,R}&=\mathrm{i}em_{\psi_i}[\not{k},\gamma_\rho]P_{L,R}.
\end{aligned} \tag{9}$$

By applying the equations of motion to the outer fermions, we obtain the relations in the effective Lagrangian [18]:

$$\begin{aligned}
&C_2^RO_2^R+C_2^LO_2^L+C_2^{L*}O_3^R+C_2^{R*}O_3^L+C_6^RO_6^R+C_6^{R*}O_6^L\\
&\Rightarrow\left(C_2^R+\frac{m_{\psi_j}}{m_{\psi_i}}C_2^{L*}+C_6^R\right)O_6^R+\left(C_2^{R*}+\frac{m_{\psi_j}}{m_{\psi_i}}C_2^L+C_6^{R*}\right)O_6^L\\
&=em_{\psi_i}\Re\left(C_2^R+\frac{m_{\psi_j}}{m_{\psi_i}}C_2^{L*}+C_6^R\right)\bar{\psi}_i\sigma^{\mu\nu}\psi_jF_{\mu\nu}\\
&\quad+\mathrm{i}em_{\psi_i}\Im\left(C_2^R+\frac{m_{\psi_j}}{m_{\psi_i}}C_2^{L*}+C_6^R\right)\bar{\psi}_i\sigma^{\mu\nu}\gamma_5\psi_jF_{\mu\nu},
\end{aligned} \tag{10}$$

and comparing Eqs. (7) and (10), we obtain

$$\mu_{ij} = 4m_e m_{\psi_i} \Re\left(C_2^R + \frac{m_{\psi_j}}{m_{\psi_i}} C_2^{L*} + C_6^R\right)\mu_B,$$
$$\epsilon_{ij} = 4m_e m_{\psi_i} \Im\left(C_2^R + \frac{m_{\psi_j}}{m_{\psi_i}} C_2^{L*} + C_6^R\right)\mu_B, \tag{11}$$

where $\Re(\cdots)$ and $\Im(\cdots)$ are the real and imaginary parts of the complex numbers, respectively, $\mu_B = e/(2m_e)$, and m_e is the electron mass. The Wilson coefficients ($C_2^R, C_2^L, C_6^R, C_6^L$) employed in this study are included in Appendix B.

We investigated the $\nu_j \to \nu_i\gamma$ processes related to the transition magnetic moment of neutrino in $U(1)_X$SSM. The amplitude of $\nu_j \to \nu_i\gamma$ can be obtained from the Feynman diagrams shown in Fig. 1. After calculating the one on the left in Fig. 1 in connection with Eq. (9), we obtain

$$\begin{aligned}\mathcal{M} = &-\mathrm{i}\int \frac{\mathrm{d}^D k}{(2\pi)^D}\frac{1}{(k^2-m_F^2)(k^2-m_S^2)^2}\\ &\times\left\{-\frac{1}{4}\left(\frac{k^2}{k^2-m_S^2}-\frac{k^4}{(k^2-m_S^2)^2}\right)\right.\\ &\left.\times(O_2^L+O_3^L)A_R B_L - \frac{1}{2}\left(1-\frac{k^2}{k^2-m_S^2}\right)O_6^L A_L B_L\right\},\end{aligned} \tag{12}$$

where k is the photon momentum, m_F corresponds to the chargino mass, andm_S corresponds to the scalar lepton mass. A_L, A_R, B_R, and B_L are

$$\begin{aligned}A_L &= -g_2 U_{j1}^* \sum_{a=1}^{3} U_{ia}^{V,*} Z_{ka}^E + U_{j2}^* \sum_{a=1}^{3} U_{ia}^{V,*} Y_{e,a} Z_{k,(3+a)}^E,\\ A_R &= \sum_{a=1}^{3} Y_{\nu,a}^* U_{i,(3+a)}^V Z_{ka}^E V_{j2},\\ B_R &= A_L^*, \quad B_L = A_R^*.\end{aligned} \tag{13}$$

Through the general description of the electromagnetic form factors of Dirac and Majorana neutrinos, we obtain the MDM and EDM for Majorana neutrinos:

$$\mu_{ij}^M = \mu_{ij}^D - \mu_{ji}^D, \qquad \epsilon_{ij}^M = \epsilon_{ij}^D - \epsilon_{ji}^D. \tag{14}$$

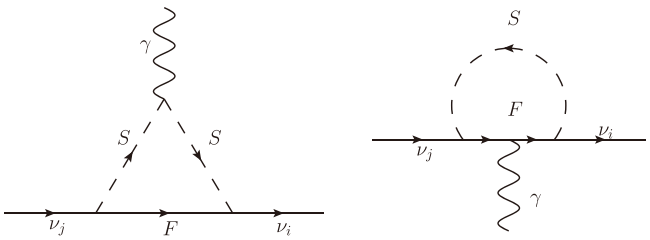

Fig. 1. Feynman diagrams for the $\nu_j \to \nu_i\gamma$ processes in $U(1)_X$ SSM

Finally, we simplify Eq. (12) and use numerical calculation software (Mathematica) to obtain numerical results.

IV. NUMERICAL ANALYSIS

In this section, we analyze the following experimental constraints:

1. The lightest CP-even Higgs h^0 mass is approximately 125.1 GeV. The Higgs h^0 decays ($h^0 \to \gamma+\gamma$, $Z+Z$, $W+W$, $b+\bar{b}$, $\tau+\bar{\tau}$) can well meet the latest experimental constraints [19–21].

The mass of the lightest CP-even Higgs boson should consider the stop quark contributions at loop level [22, 23]:

$$m_h^0 = \sqrt{(m_{h_1}^0)^2 + \Delta m_h^2}, \tag{15}$$

where $m_{h_1}^0$ represents the lightest tree-level Higgs boson mass. The concrete form of Δm_h^2 is

$$\begin{aligned}\Delta m_h^2 &= \frac{3m_t^4}{4\pi^2 v^2}\left[\left(\tilde{t}+\frac{1}{2}\tilde{X}_t\right)+\frac{1}{16\pi^2}\left(\frac{3m_t^2}{2v^2}-32\pi\alpha_3\right)\left(\tilde{t}^2+\tilde{X}_t\tilde{t}\right)\right],\\ \tilde{t} &= \log\frac{M_{\tilde{T}}^2}{m_t^2}, \qquad \tilde{X}_t = \frac{2\tilde{A}_t^2}{M_{\tilde{T}}^2}\left(1-\frac{\tilde{A}_t^2}{12M_{\tilde{T}}^2}\right).\end{aligned} \tag{16}$$

α_3 is the strong coupling constant. $M_{\tilde{T}} = \sqrt{m_{\tilde{t}_1} m_{\tilde{t}_2}}$ and $m_{\tilde{t}_{1,2}}$ are the stop masses. $\tilde{A}_t = A_t - \mu\cot\beta$ and A_t is the trilinear Higgs stop coupling. We used the values of these parameter to fix $m_h^0 \sim 125.1$GeV.

The mass matrix of chargino includes the parameters v_u, v_d, λ_H, v_S, and the mass squared matrix of scalar lepton includes v_u, v_d, λ_H, v_S, v_η, $v_{\bar{\eta}}$, g_X, g_{YX}. The CP-even Higgs mass squared matrix at tree level also has these parameters. Given that we fit the CP-even Higgs h^0 mass, the values of these parameters become restricted. In general, these parameters affect the mass matrix of charginos and the mass squared matrix of scalar leptons. Therefore, they have effects on the neutrino transition magnetic moment.

2. The constraints from neutrino experiment data including mixing angles and mass variances were considered in our numerical analysis [24–26].

3. The Z' boson mass is larger than 5.1 TeV. The gauge boson masses are [13]

$$\begin{aligned}M_\gamma^2 &= 0,\\ M_{Z,Z'}^2 &= \frac{1}{8}\left((g_1^2+g_2^2+g_{YX}^2)v^2+4g_X^2\xi^2\right.\\ &\left.\mp\sqrt{(g_1^2+g_2^2+g_{YX}^2)^2v^4+8(g_{YX}^2-g_1^2-g_2^2)g_X^2v^2\xi^2+16g_X^4\xi^4}\right).\end{aligned} \tag{17}$$

For $M_{Z'}$, the corresponding expression can be notably

simplified under the supposition $\xi^2 \gg v^2$. It can be demonstrated that

$$\begin{aligned} M_{Z'}^2 &= \frac{1}{8}\Big((g_1^2+g_2^2+g_{YX}^2)v^2+4g_X^2\xi^2 \\ &\quad + \sqrt{(g_1^2+g_2^2+g_{YX}^2)^2v^4+8(g_{YX}^2-g_1^2-g_2^2)g_X^2v^2\xi^2+16g_X^4\xi^4}\Big) \\ &\approx \frac{1}{8}\Big(4g_X^2\xi^2+\sqrt{16g_X^4\xi^4}\Big) \\ &= g_X^2\xi^2. \end{aligned} \tag{18}$$

$M_{Z'}/g_X > 6$ TeV expresses the results for the particle [27].

4. The neutralino mass is limited to more than 116 GeV, the chargino mass is limited to more than 1000 GeV, and the slepton mass is limited to more than 600 GeV [19].

According to these experimental constraints, we generally set the values of new mass parameters ($M_{BB'}$,M_{BL},M_S) around the energy scale of new physics (10^3 GeV). $M_{\tilde{L}}$ and $M_{\tilde{E}}$ are of mass square dimension and can reach the order of 10^6 GeV^2. Non-diagonal elements of the scalar lepton mass matrix affect T_e, which can reach 10^{-1} GeV. tanβ and v_S affect the mass matrix of chargino. $v_{\bar{\eta}}$ and v_η affect the slepton mass. The loop diagram is produced by the chargino and scalar lepton. We adopted the following parameter values, which can affect the neutrino transition magnetic moment in the numerical calculations:

$$\begin{aligned} &\tan\beta = 23, \quad v_S = 4.3\ \text{TeV}, \quad \tan\beta_\eta = \frac{v_{\bar{\eta}}}{v_\eta} = 0.8, \\ &v_{\bar{\eta}} = 17\sin(\beta_\eta)\ \text{TeV}, \quad v_\eta = 17\cos(\beta_\eta)\ \text{TeV}, \\ &T_{e11} = T_{e22} = T_{e33} = 0.5\ \text{GeV}, \\ &M_{\tilde{L}11} = M_{\tilde{L}22} = M_{\tilde{L}33} = 3\ \text{TeV}^2, \\ &M_{\tilde{E}11} = M_{\tilde{E}22} = M_{\tilde{E}33} = 8\ \text{TeV}^2. \end{aligned} \tag{19}$$

The parameters we selected are of good universality. The parameters we examine in the following numerical analysis include

$$g_X,\quad \lambda_H,\quad M_2,\quad \mu,\quad g_{YX}. \tag{20}$$

Unless specifically stated, the non-diagonal elements of the parameters are supposed to be zero.

A. Neutrino Mixing

In the neutrino mass matrix, elements such as Y_ν are relevant to neutrino mixing. The transition magnetic moment is closely related to the mass matrix including Y_ν. In this subsection, we use a top-down approach to derive the formulae for the neutrino mass and mixing angle from the effective neutrino mass matrix. We adopted the normal ordering spectrum to calculate the neutrino observables ($\sin^2(\theta_{ij})$ *etc.*). The procedure is detailed in Appendix C.

The constraints from neutrino experimental data are [19]

$$\begin{aligned} &\sin^2(\theta_{12}) = 0.307^{+0.013}_{-0.012}, \\ &\sin^2(\theta_{23}) = 0.546\pm0.021, \\ &\sin^2(\theta_{13}) = 0.022\pm0.0007, \\ &\Delta m^2_\odot = (7.53\pm0.18)\times10^{-5}\ \text{eV}^2, \\ &|\Delta m^2_A| = (2.453\pm0.033)\times10^{-3}\ \text{eV}^2. \end{aligned} \tag{21}$$

To fit the data of neutrino physics, we set the parameters as

$$\begin{aligned} &Y_{X11} = Y_{X22} = Y_{X33} = 0.1, \quad Y_{\nu_{22}} = 1.4000\times10^{-6}, \\ &Y_{\nu_{33}} = 1.352420\times10^{-6}, \qquad Y_{\nu_{12}} = 7.604202\times10^{-8}. \end{aligned} \tag{22}$$

By fixing some matrix elements in Eq. (22) and taking others as variables, discussion on data is facilitated.

In Fig. 2, $\sin^2(\theta_{12})$, $\sin^2(\theta_{23})$, and 10 $\sin^2(\theta_{13})$ are plotted in the plane of $Y_{\nu23}$ versus $Y_{\nu13}$. If the area satisfies 10 $\sin^2(\theta_{13})$ in 30σ, it clearly satisfies $\sin^2(\theta_{23})$ in 3σ. With $Y_{\nu_{11}} = 1.092847\times10^{-6}$, the constraints of three mixing angles are satisfied (they are all in the range of 3σ). The yellow, blue, and green areas represent $0.483 < \sin^2(\theta_{23}) < 0.609$, $0.271 < \sin^2(\theta_{12}) < 0.346$, and $0.199 < 10\sin^2(\theta_{13}) < 0.241$, respectively. The yellow re-

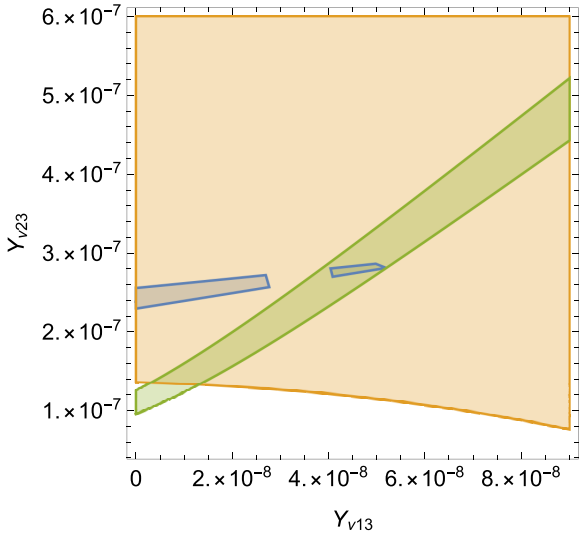

Fig. 2. (color online) $\sin^2(\theta_{12})$, $\sin^2(\theta_{23})$, and 10 $\sin^2(\theta_{13})$ plotted in the plane of $Y_{\nu13}$ versus $Y_{\nu23}$. The yellow, blue, and green areas represent $0.483 < \sin^2(\theta_{23}) < 0.609$, $0.271 < \sin^2(\theta_{12}) < 0.346$, and $0.199 < 10\sin^2(\theta_{13}) < 0.241$, respectively.

gion resembles a rectangle, the blue region resembles a fragmented ribbon, and the green region resembles a continuous ribbon. The overlapping area represents values of $Y_{\nu 23}$ and $Y_{\nu 13}$ that satisfy all three mixing angle constraints.

Similarly, in Fig. 3, the three constraints on the mixing angles are satisfied (they are all in the range of 3σ). $\Delta m^2_{\odot}$ and $|\Delta m^2_A|$ are plotted in the plane of $Y_{\nu 23}$ versus $Y_{\nu 13}$. The yellow area represents $2.353\times10^{-21}\ \mathrm{eV}^2 < |\Delta m^2_A| < 2.553\times10^{-21}\ \mathrm{eV}^2$, which resembles a rectangle. The blue area represents $6.99\times10^{-23}\ \mathrm{eV}^2 < \Delta m^2_{\odot} < 8.07\times10^{-23}\ \mathrm{eV}^2$, which resembles a band. Overall, the overlapping part is needed.

In Fig. 4, we combine Figs. 2 and 3 to find a reasonable parameter space. The overlapping area in Fig. 2 satisfies $0.483 < \sin^2(\theta_{23}) < 0.609$, $0.271 < \sin^2(\theta_{12}) < 0.346$, and $0.199 < 10\sin^2(\theta_{13}) < 0.241$. In Fig. 3, the overlapping area satisfies $1.2\times10^{-21}\ \mathrm{eV}^2 < |\Delta m^2_A| < 4.3\times10^{-21}\ \mathrm{eV}^2$ and $7.3\times10^{-23}\ \mathrm{eV}^2 < \Delta m^2_{\odot} < 9.9\times10^{-23}\ \mathrm{eV}^2$. In this figure, all shadow overlapping areas meet five constraints.

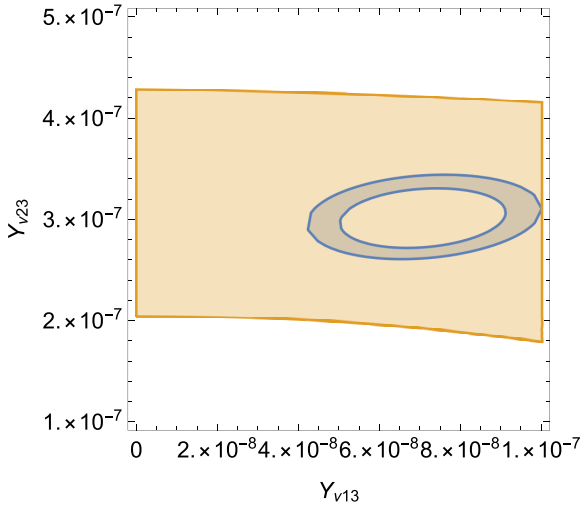

Fig. 3. (color online) $\Delta m^2_{\odot}$ and $|\Delta m^2_A|$ plotted in the plane of $Y_{\nu 13}$ versus $Y_{\nu 23}$. The yellow area represents $1.2\times10^{-21}\ \mathrm{eV}^2 < |\Delta m^2_A| < 4.3\times10^{-21}\ \mathrm{eV}^2$, and the blue area represents $7.3\times10^{-23}\ \mathrm{eV}^2 < \Delta m^2_{\odot} < 9.9\times10^{-23}\ \mathrm{eV}^2$.

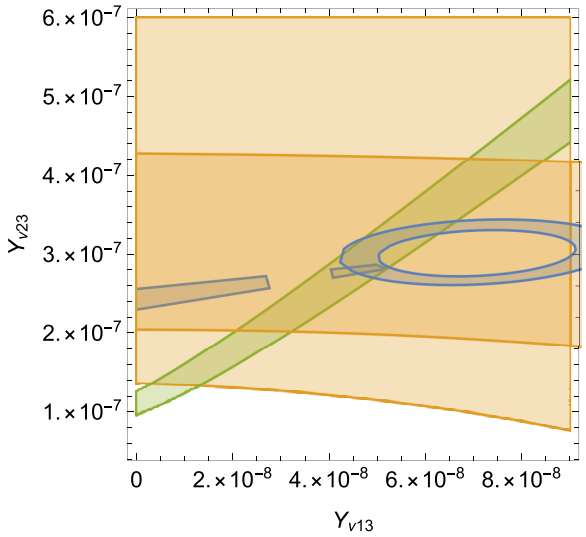

Fig. 4. (color online) Combining Figs. 2 and 3, the overlapping area satisfies all constraints.

Next, we discuss how a matrix element Y_{ν} such as $Y_{\nu_{11}}$ affects $\sin^2(\theta_{12})$, $\sin^2(\theta_{23})$, and $10\times\sin^2(\theta_{13})$. In Fig. 5, the constraints on two mass variances are satisfied. Then, $\sin^2(\theta_{12})$, $\sin^2(\theta_{23})$, and $10\times\sin^2(\theta_{13})$ are plotted as $Y_{\nu 11}$ varies. According to the analysis of Fig. 4, we set $Y_{\nu_{13}} = 4.516926\times10^{-8}$ and $Y_{\nu_{23}} = 2.803229\times10^{-7}$. According to the aforementioned data, the blue, yellow, and green regions correspond to the values of $\sin^2(\theta_{12})$, $\sin^2(\theta_{23})$, and $10\times\sin^2(\theta_{13})$ mixing angles in the 3σ range, respectively. The blue line represents $\sin^2(\theta_{12})$. It grows consistently from $Y_{\nu_{11}} = 1.0\times10^{-6}$ to $Y_{\nu_{11}} = 1.3\times10^{-6}$, with rapid growth from $Y_{\nu_{11}} = 1.07\times10^{-6}$ to $Y_{\nu_{11}} = 1.136\times10^{-6}$. However, it remains almost constant in the $Y_{\nu_{11}}$ region $[1.3\times10^{-6}, 1.5\times10^{-6}]$. The yellow line represents $\sin^2(\theta_{23})$. We found that it remains stable in the range from $Y_{\nu_{11}} = 1.0\times10^{-6}$ to $Y_{\nu_{11}} = 1.5\times10^{-6}$, which is always in the range of 3σ. The green line represents $10\times\sin^2(\theta_{13})$. With the increase in $Y_{\nu_{11}}$, $10\times\sin^2(\theta_{13})$ grows increasingly fast. We conclude that, to satisfy the mixing angle experimentally measured, $Y_{\nu 11}$ must be set between two pink lines. Therefore, $Y_{\nu 11}$ should be one of the values in the range from 1.08902×10^{-6} to 1.9701×10^{-6}.

Using the Gaussian likelihood function, we constructed a function combining three mixing angles and two mass variances:

$$p(\mathbf{y}) = \prod_{i=1}^{5} \frac{1}{\sqrt{2\pi\sigma_i^2}} \exp\left(-\frac{(y_i-\mu_i)^2}{2\sigma_i^2}\right), \tag{23}$$

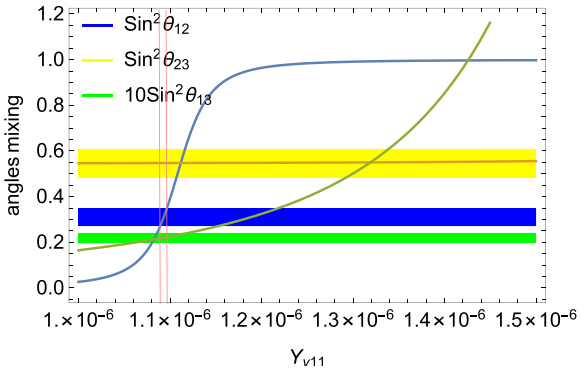

Fig. 5. (color online) $\sin^2(\theta_{12})$, $\sin^2(\theta_{23})$, and $10\times\sin^2(\theta_{13})$ are plotted as $Y_{\nu 11}$ varies. The blue line represents $\sin^2(\theta_{12})$. The yellow line represents $\sin^2(\theta_{23})$. The green line represents $10\times\sin^2(\theta_{13})$. The blue, yellow, and green regions correspond to the values of the $\sin^2(\theta_{12})$, $\sin^2(\theta_{23})$, and $10\times\sin^2(\theta_{13})$ mixing angles in the 3σ range. The pink lines represent the overlapping satisfaction interval.

where y_i and μ_i from 1 to 5 represent three mixing angles and two mass variances, respectively. We set

$$\begin{aligned}
&\mu_1 = \sin^2(\theta_{12}) = 0.307,\\
&\mu_2 = \sin^2(\theta_{23}) = 0.546,\\
&\mu_3 = \sin^2(\theta_{13}) = 0.022,\\
&\mu_4 = \Delta m^2_{\odot} = 7.53\times10^{-5}\ \mathrm{eV}^2,\\
&\mu_5 = |\Delta m^2_A| = 2.453\times10^{-3}\ \mathrm{eV}^2.
\end{aligned} \tag{24}$$

σ_i denotes their standard deviation. The extreme value of the ordinate in Fig. 6 corresponds to the value of our parameter. We set $Y_{\nu_{11}} = 1.092847\times10^{-6}$.

In summary, combining the five experimental constraints on neutrinos, we determined the range of values for our selected parameters. From the conducted analysis, we determined that the following parameter values are reasonable:

$$\begin{aligned}
&Y_{\nu_{11}} = 1.092847\times10^{-6},\ Y_{\nu_{22}} = 1.4000\times10^{-6},\\
&Y_{\nu_{33}} = 1.352420\times10^{-6},\ Y_{\nu_{12}} = 7.604202\times10^{-8},\\
&Y_{\nu_{13}} = 4.516926\times10^{-8},\ Y_{\nu_{23}} = 2.803229\times10^{-7}.
\end{aligned} \tag{25}$$

B. Processes of $\nu_j \to \nu_{i\gamma}$

One of the objectives of this study was to elucidate the influence of certain sensitive parameters on the numerical results of the neutrino transition magnetic moment μ^M_{ij} under experimental constraints. We used Eq. (25) for further numerical calculations. Besides, μ^M_{ij} was used to represent the transition magnetic moment of the Majorana neutrinos. We set a number of parameters such as g_X, λ_H, M_2, and μ and investigated them as extensively as possible

g_X is the gauge coupling constant of the new gauge group $U(1)_X$. Besides, the mass matrices of slepton and coupling vertices $\nu_i\chi_j^-\tilde{e}_k^*$ all include the important parameter g_X, which can improve the new physics effect. We show the results forg_X and μ^M_{12}/μ_B in Fig. 7 (a), in which the dashed line corresponds to $\lambda_H = 0.3$ and the solid line corresponds to $\lambda_H = 0.1$. Here, we set $\mu = 1000$ GeV and $M_2 = 1200$ GeV. We found that both lines increase in most of the region of g_X throughout the range 0.3−0.51. Note also that the solid line is larger than the dashed line. Generally speaking, a larger g_X should lead to larger UMSSM contributions.

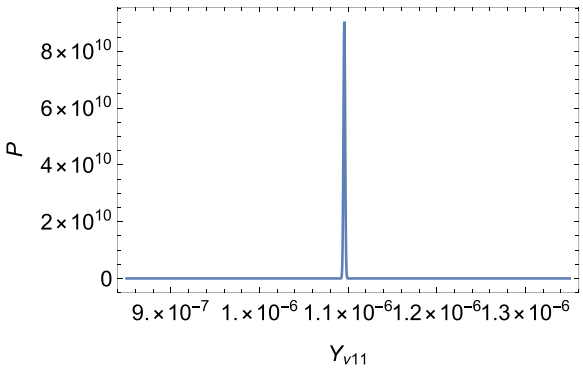

Fig. 6. (color online) Relationship between $Y_{\nu_{11}}$ and P.

In Fig. 7 (b), where$g_X = 0.5$ (dashed line) and $g_X = 0.3$ (solid line), we set $\lambda_H = 0.1$ and $M_2 = 1200$ GeV. As the solid and dashed lines go from bottom to top, μ^M_{12}/μ_B increases as g_X increases. They are decreasing functions of μ; μ appears in the term $\frac{1}{\sqrt{2}}\lambda_H v_S + \mu$ in the mass matrix for the chargino, which may affect the results. As shown in Fig. 7 (b), with the increase of μ, the chargino mass becomes heavier, which suppresses the numerical results.

λ_H comes from the term $\lambda_H\hat{S}\hat{H}_u\hat{H}_d$ in the superpotential. The mass matrices of several particles (chargino, neutralino) include the important parameter λ_H, which possibly produces complex effects on the numerical results. In Fig. 7 (c), we set $\mu = 1000$ GeV and $g_X = 0.3$. The solid and dashed lines represent $M_2 = 1200$ GeV and $M_2 = 2400$ GeV, respectively. Both the dashed and solid lines are decreasing functions as λ_H increases.

In Fig. 7 (d), we set $\lambda_H = 0.1$ and g_X=0.3. The solid and dashed lines represent $\mu = 1000$ GeV and $\mu = 1200$ GeV, respectively. Similarly, M_2, as the mass matrix element of chargino, has an effect similar to that of μ on μ^M_{12}/μ_B. Note also that μ^M_{12}/μ_B decreases as M_2 increases.

The above discussion concerns μ^M_{12}/μ_B. For μ^M_{13}/μ_B and μ^M_{23}/μ_B, the influence of certain sensitive parameters is similar to that of μ^M_{12}/μ_B. Therefore, we only list some of the parameters and plot their effects.

Figures 8 (a) and 8 (b) describe the relationship between g_X and μ^M_{13}/μ_B and μ^M_{23}/μ_B. Similar to the description of μ^M_{13}/μ_B, the dashed line corresponds to $\lambda_H = 0.3$ and the solid line corresponds to $\lambda_H = 0.1$. For $\mu = 1000$ GeV and $M_2 = 1200$ GeV, the effects of g_X on the different components of μ^M_{ij}/μ_B exhibit similar trends. In Fig. 8 (a), within the value range, the maximum values for solid and dashed lines are 3.27×10^{-19} and 1.92×10^{-19}, respectively. In Fig. 8 (b), the maximum values for solid and dashed lines are 7.04×10^{-20} and 4.12×10^{-20}.

Figures 8 (c) and 8 (d) show the influences of M_2 on μ^M_{13}/μ_B and μ^M_{23}/μ_B. Similar trends are observed: decreasing functions of M_2. In Fig. 8 (c), the maximum values for the solid and dashed lines are 1.69×10^{-19} and 1.55×10^{-19}, respectively. The maximum values for the dashed and solid lines in Fig. 8 (d) are 3.10×10^{-19} and 4.03×10^{-20}, respectively.

We conclude from the above graphs that μ^M_{ij}/μ_B increases with g_X and decreases with μ, λ_H, and M_2. Their

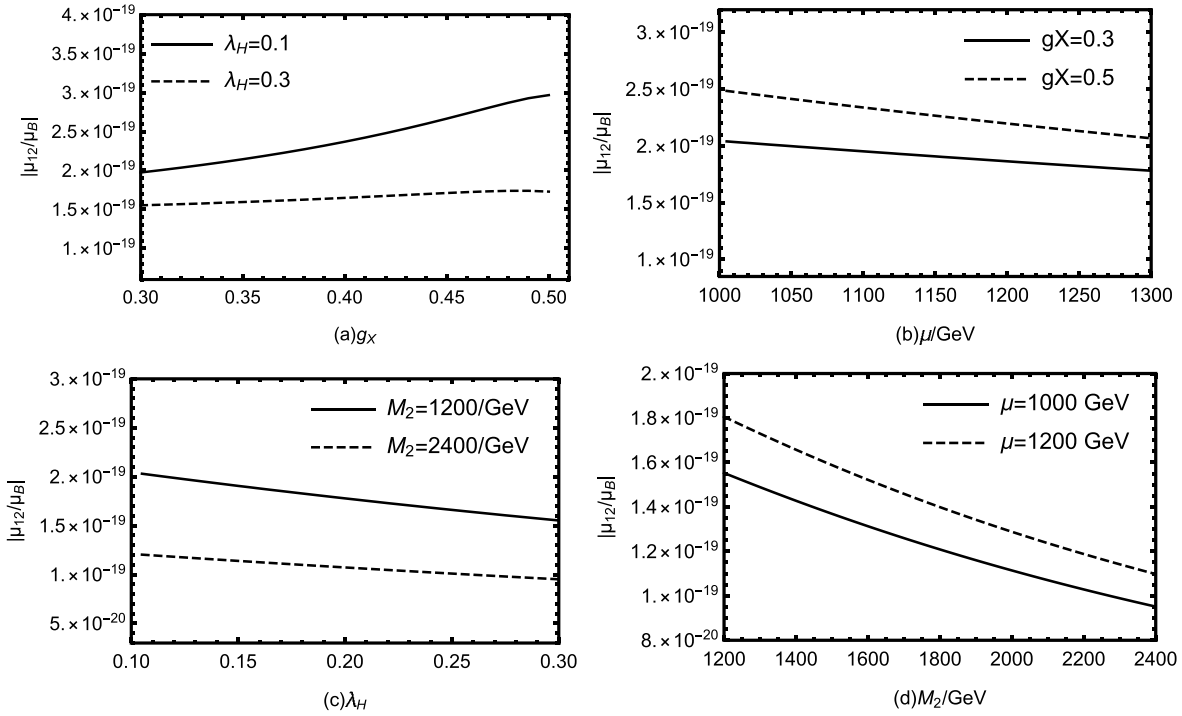

Fig. 7. Relationships between different parameters and μ_{12}^M/μ_B.

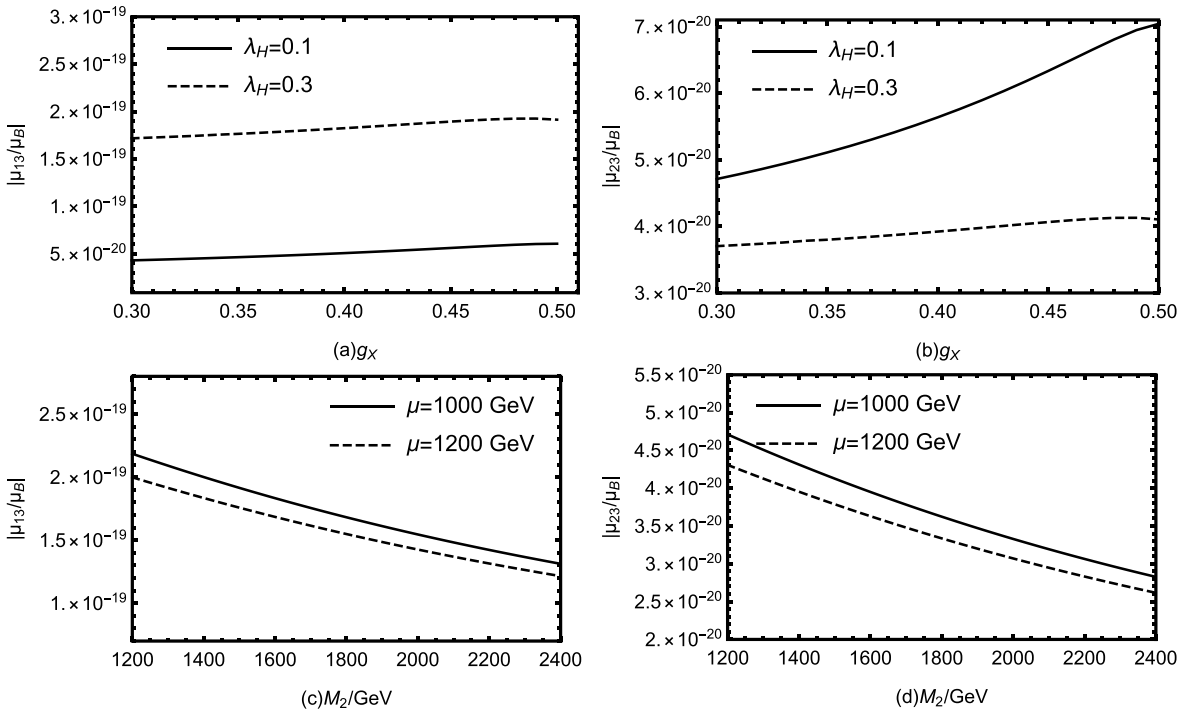

Fig. 8. Relationships of different parameters with μ_{13}^M/μ_B and μ_{23}^M/μ_B.

influences on μ_{ij}^M/μ_B tend to be similar. Overall, g_X, λ_H, μ, and M_2 are sensitive parameters that have an evident impact on μ_{ij}^M/μ_B.

To properly explore the μ_{ij}^M parameter spaces, we generated scatter diagrams for several parameters, as shown in Fig. 9. The scanned parameters are listed in Table 2. We use ■ ($\mu_{12}^M/\mu_B < 1.6\times10^{-19}$), ♦ ($1.6\times10^{-19} \le \mu_{12}^M/\mu_B < 1.9\times10^{-19}$), ▲ ($1.9\times10^{-19} \le \mu_{12}^M/\mu_B < 2.2\times10^{-19}$), and ● $2.2\times10^{-19} \le \mu_{12}^M/\mu_B < 3.2\times10^{-19}$) to represent the results of the transition magnetic moment.

Figure 9 (a) shows scatter plots of M_2 versus μ_{12}^M/μ_B. The figure resembles a parallelogram. We can see that

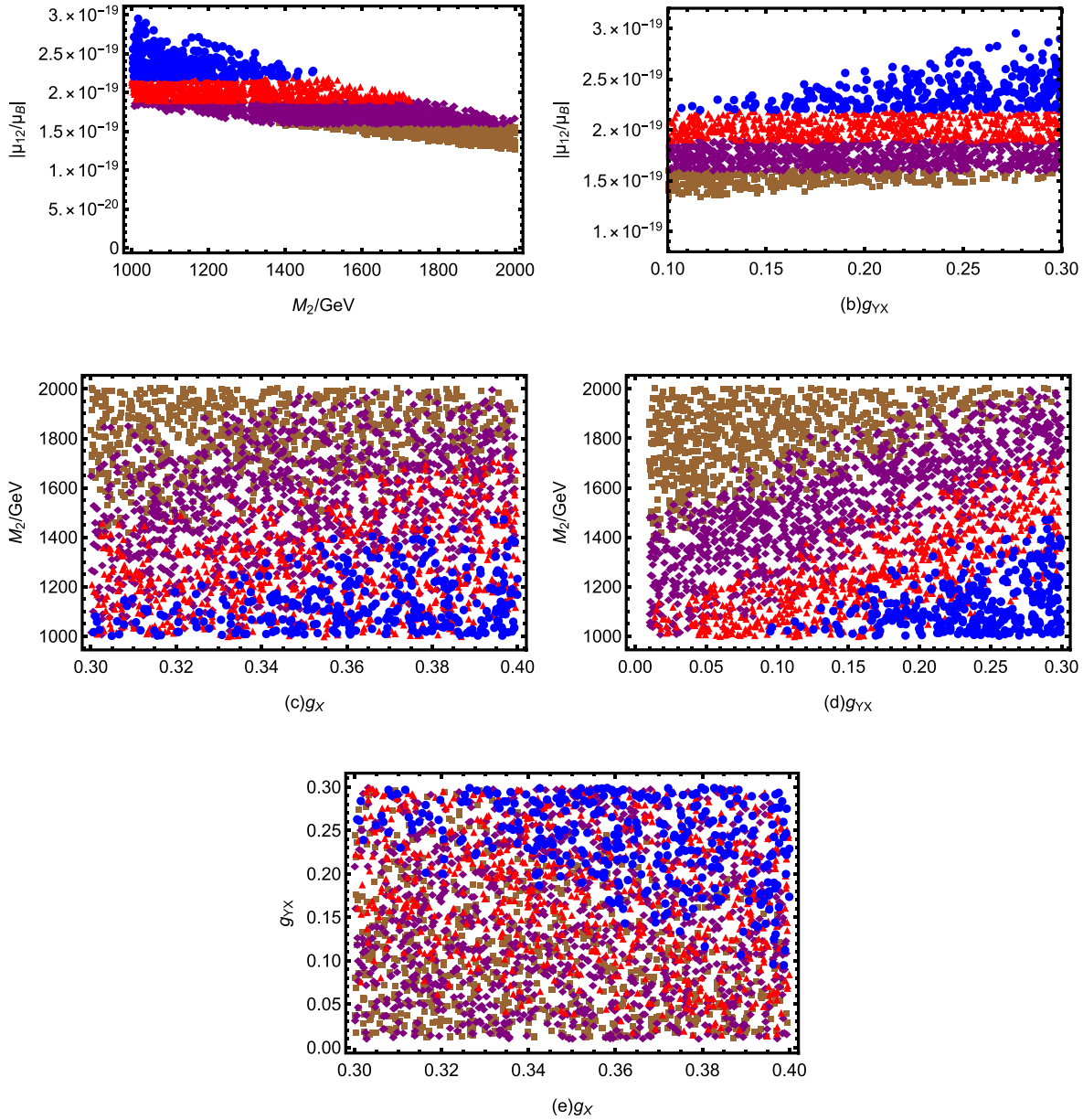

Fig. 9. (color online) Relationships between different parameters and μ_{12}^M/μ_B.

Table 2. Scanning parameters employed in Fig. 9.

Parameters	g_X	g_{YX}	M_2/GeV
Min	0.3	0.01	1000
Max	0.4	0.3	2000

● is at the top, ▲ and ♦ are in the middle and ▲ is on top of ♦. Finally ■ is at the bottom. Note that μ_{12}^M/μ_B decreases as M_2 increases, and its maximum value is 3.0×10^{-19}. This result is consistent with the result of line μ_{12}^M/μ_B. Figure 9 (b) shows scatter plots of g_{YX} versus μ_{12}^M/μ_B. It has the same graphic color layout as Fig. 9 (a) but with a different trend. It can be observed that the value of μ_{12}^M/μ_B increases as g_{YX} increases.

Figure 9 (c) shows the effects of g_X and M_2 on μ_{12}^M/μ_B. Different values of μ_{12}^M/μ_B in the parameter space exhibit clear stratification. The upper left corner is ■, followed by ♦, immediately followed by ▲, and to the bottom right by ●. From the trend in this graph, we conclude that μ_{12}^M/μ_B reaches its maximum value when g_X = 0.4 and M_2= 1000 within the parameter space of Fig. 9 (c). In Fig. 9 (d), the graphical distribution is similar to that of Fig. 9 (c). This demonstrates that the effects of g_{YX} and g_X on μ_{12}^M/μ_B are similar.

Figure 9 (e) allows deriving the effects of g_X and g_{YX} on μ_{12}^M/μ_B. The color distribution is evident: the upper right corner is a mix of blue, red, and purple with some amount of brown. The lower left corner is a mix of red,

brown, and purple colors. The red color is less distributed in the lower left corner. Note that the larger values of μ^M_{12}/μ_B are concentrated in the upper right corner, which means that an increase in g_X and g_{YX} promotes its increase.

V. CONCLUSIONS

In this study, we first introduced $U(1)_X$SSM and then analyzed the neutrino transport magnetic moment on this basis. We studied the transition magnetic moment of the Majorana neutrinos by applying the effective Lagrangian method and on-shell scheme. We derived the Feynman diagrams and calculated the neutrino transport moment by combining the operators. We conducted a theoretical analysis on neutrino mixing. Based on the five bounds of the neutrino experiment, we filtered for the right effective light neutrino mass matrix element. In addition, we performed a large number of numerical calculations and plotted graphs for different parameters versus μ_{ij} according to the experimental limits, followed by a large scan that yielded rich numerical results. In the numerical calculations, we first fit the experimental data on neutrino mass variance and mixing angle for the normal order condition. Then, we selected some sensitive parameters, including g_X, λ_H, M_2, μ, and g_{YX}. Using one dimensional plots, we analyzed parameters such asg_X, λ_H, M_2, and μ versus μ^M_{ij}/μ_B. In scatter plots, we selected three variants in Table 2 for further study. By analyzing the numerical results, we elucidated the relationship between the selected parameters and μ^M_{ij}/μ_B, concluding that they are sensitive parameters.

Moreover, we concluded that the order of magnitude of μ^M_{ij}/μ_B is between 10^{-20} and 10^{-19}. From the diagrams, we found that the numerical value for μ^M_{12}/μ_B is on the order of 10^{-19}. Better limits on the neutrino transition magnetic moment were recently reported from the XENONnT experiment [28]. We present the bounds at 90% and 99% C.L in Table 3. The experimental sensitivity for $|\mu_{ij}/\mu_B|$ with $i \neq j$ is slightly smaller than 10^{-11}. In a Type-II radiative seesaw scenario [29], the authors investigated the neutrino magnetic moment; their numerical results indicated that $|\mu_{ij}/\mu_B|$ is large and can reach 10^{-12}. Our corresponding results are on the order of 10^{-19}, which is a much smaller value [29].

Compared with other conclusions [10], our results are two orders of magnitude larger. The reason is that $U(1)_X$SSM has new gauge couplings, namely g_X and g_{YX}. The vertices of ν_i-χ^-_j-$\tilde{e}^*_k$ are included in Eq. (37). Accordingly, Yukawa couplings ($Y_{e,a}$ and $Y_{\nu,a}$) and gauge coupling g_2 are included in the above equation. $Y_{\nu,a}$ values are extremely small, whereas $Y_{e,a}$ values are small. This is the case of $Y_{e,2}$ for muons; with $\tan\beta = 10$, the value of $Y_{e,2}$ is approximately 0.006, which is much smaller than g_2. g_X and g_{YX} appear in the mass squared matrix of scalar leptons, and their effects are embedded in the rotation matrix Z^E. Therefore, the new gauge couplings g_X and g_{YX} can produce new effects. Furthermore, the right-handed neutrinos and three Higgs singlets are added. They can also produce new effects and improve the numerical results.

Table 3. Limits on neutrino transition magnetic moment at XENONnT experiment.

XENONnT	90% C.L	99% C.L
$\|\mu_{12}/\mu_B\|$	$< 6.77\times10^{-12}$	$< 9.63\times10^{-12}$
$\|\mu_{13}/\mu_B\|$	$< 6.98\times10^{-12}$	$< 9.94\times10^{-12}$
$\|\mu_{23}/\mu_B\|$	$< 9.04\times10^{-12}$	$< 12.9\times10^{-12}$

APPENDIX A

The mass matrix for chargino reads

$$m_{\tilde{\chi}^-} = \begin{pmatrix} M_2 & \frac{1}{\sqrt{2}}g_2 v_\mu \\ \frac{1}{\sqrt{2}}g_2 v_d & \frac{1}{\sqrt{2}}\lambda_H v_S + \mu \end{pmatrix}. \tag{A1}$$

This matrix is diagonalized by U and V:

$$U^* m_{\chi^-} V^\dagger = m^{dia}_{\chi^-}, \tag{A2}$$

with

$$\begin{aligned} \tilde{W}^- &= \sum_{t_2} U^*_{j1}\lambda^-_j, \quad \tilde{H}^-_d = \sum_{t_2} U^*_{j2}\lambda^-_j, \\ \tilde{W}^+ &= \sum_{t_2} V^*_{1j}\lambda^+_j, \quad \tilde{H}^-_u = \sum_{t_2} V^*_{2j}\lambda^+_j. \end{aligned} \tag{A3}$$

The mass matrix for slepton reads

$$m^2_{\tilde{e}} = \begin{pmatrix} m_{\tilde{e}_L\tilde{e}^*_L} & \frac{1}{2}(\sqrt{2}v_d T^\dagger_e - v_u(\lambda_H v_s + \sqrt{2}\mu)Y^\dagger_e) \\ \frac{1}{2}(\sqrt{2}v_d T_e - v_u Y_e(\sqrt{2}\mu^* + v_s\lambda_H{}^*) & m_{\tilde{e}_R\tilde{e}^*_R} \end{pmatrix}. \tag{A4}$$

$$m_{\tilde{e}_L\tilde{e}_L^*} = M_{\tilde{L}}^2 + \frac{1}{8}\Big((g_1^2+g_{YX}^2)(-v_u^2+v_d^2) + g_{YX}g_X(-2v_{\bar{\eta}}^2+2v_\eta^2-v_u^2+v_d^2); +g_2^2(-v_d^2+v_u^2)\Big) + \frac{1}{2}v_d^2 Y_e^\dagger Y_e, \tag{A5}$$

$$m_{\tilde{e}_R\tilde{e}_R^*} = M_{\tilde{E}}^2 - \frac{1}{8}\Big(2(g_1^2+g_{YX}^2)(-v_u^2+v_d^2) + g_{YX}g_X(3v_d^2-3v_u^2-4v_{\bar{\eta}}^2+4v_\eta^2) + g_X^2(-2v_{\bar{\eta}}^2+2v_\eta^2-v_u^2+v_d^2)\Big) + \frac{1}{2}v_d^2 Y_e Y_e^\dagger. \tag{A6}$$

This matrix is diagonalized by Z^E:

$$Z^E m_{\tilde{e}}{}^2 Z^{E,\dagger} = m_{2,\hat{e}}^{\rm dia}, \tag{A7}$$

with

$$\tilde{e}_{L,i} = \sum_j Z_{ji}^{E,*}\tilde{e}_j, \quad \tilde{e}_{R,i} = \sum_j Z_{ji}^{E,*}\tilde{e}_j. \tag{A8}$$

The mass matrix for neutrino reads

$$M_\nu = \begin{pmatrix} 0 & \frac{v_u}{\sqrt{2}}Y_\nu^T \\ \frac{v_u}{\sqrt{2}}Y_\nu & \sqrt{2}v_{\bar{\eta}}Y_X \end{pmatrix}. \tag{A9}$$

This matrix is diagonalized by U_V:

$$U^{V,*} m_\nu U^{V,\dagger} = m_\nu^{\rm dia}, \tag{A10}$$

with

$$\nu_{L,i} = \sum_j U_{ji}^{V,*}\lambda_{\nu,j}, \quad \nu_{R,i}^* = \sum_j U_{ji}^V \lambda_{\nu,j}^*. \tag{A11}$$

Here, we show some couplings that are required in this model. We derive the vertices of ν_i-χ_j^--$\tilde{e}_k^*$

$$\mathcal{L}_{\nu_i\chi_j^-\tilde{e}_k^*} = \bar{\nu}_i\Big\{\sum_{a=1}^3\Big(U_{j2}^* U_{ia}^{V,*} Y_{e,a} Z_{k,3+a}^E - g_2 U_{j1}^* U_{ia}^{V,*} Z_{ka}^E\Big)P_L, + \sum_{a,b=1}^3 Y_{\nu,ab}^* U_{i,3+a}^V Z_{kb}^E V_{j2} P_R\Big\}\chi_j^-\tilde{e}_k^*. \tag{A12}$$

APPENDIX B

The expressions for $C_2^R, C_2^L, C_6^R, C_6^L$ are

$$C_2^R = \sum_{j=1}^2\sum_{k=1}^6 |A_L^{ijk}|^2 F(X_{\tilde{L}_K}, X_{X_j^\pm}),$$
$$C_2^L = \sum_{j=1}^2\sum_{k=1}^6 |A_R^{ijk}|^2 F(X_{\tilde{L}_K}, X_{X_j^\pm}),$$
$$C_6^R = \sum_{j=1}^2\sum_{k=1}^6 A_R^{ijk} B_R^{ijk} G(X_{\tilde{L}_K}, X_{X_j^\pm}),$$
$$C_6^L = \sum_{j=1}^2\sum_{k=1}^6 A_L^{ijk} B_L^{ijk} G(X_{\tilde{L}_K}, X_{X_j^\pm}). \tag{B1}$$

with the functions

$$F(x,y) = \frac{1}{384\pi^2\Lambda^2}\Big(\frac{x^2-5xy-2y^2}{(x-y)^3} + \frac{6xy^2(\log x - \log y)}{(x-y)^4}\Big),$$
$$G(x,y) = \frac{1}{64\pi^2\Lambda^2}\frac{x^2-y^2+2xy(\log y - \log x)}{(x-y)^3}. \tag{B2}$$

The couplings we used are

$$A_L = \sum_{a=1}^3 (U_{j2}^* U_{ia}^{V,*} Y_{e,a} Z_{k3+a}^E - g_2 U_{j1}^* U_{ia}^{V,*} Z_{ka}^E),$$
$$A_R = \sum_{a,b=1}^3 Y_{\nu,ab}^* U_{i3+a}^V Z_{kb}^E V_{j2},$$
$$B_R = A_L^*, \quad B_L = A_R^*. \tag{B3}$$

APPENDIX C

The effective light neutrino mass matrix can be expressed as

$$\mathcal{M}_\nu^{eff} \approx -\Big(\frac{v_u Y_\nu}{\sqrt{2}}\Big)\Big(\sqrt{2}v_{\bar{\eta}}Y_X\Big)^{-1}\Big(\frac{v_u Y_\nu}{\sqrt{2}}\Big)^T. \tag{C1}$$

Using the " top-down " method [30], we obtain the Hermitian matrix:

$$\mathcal{H} = (\mathcal{M}_\nu^{\rm eff})^\dagger \mathcal{M}_\nu^{\rm eff}. \tag{C2}$$

Moreover, we can diagonalize the 3×3 matrix $\mathcal{H}$ to obtain three eigenvalues:

$$
\begin{aligned}
m_1^2 &= \frac{a}{3} - \frac{1}{3}p(\cos\phi + \sqrt{3}\sin\phi),\\
m_2^2 &= \frac{a}{3} - \frac{1}{3}p(\cos\phi - \sqrt{3}\sin\phi),\\
m_3^2 &= \frac{a}{3} + \frac{2}{3}p\cos\phi.
\end{aligned} \tag{C3}
$$

These parameters can be expressed as

$$
\begin{aligned}
&p = \sqrt{a^2 - 3b}, \quad \phi = \frac{1}{3}\arccos\left(\frac{1}{p^3}\left(a^3 - \frac{9}{2}ab + \frac{27}{2}c\right)\right),\\
&a = \mathrm{Tr}(\mathcal{H}),\\
&b = \mathcal{H}_{11}\mathcal{H}_{22} + \mathcal{H}_{11}\mathcal{H}_{33} + \mathcal{H}_{22}\mathcal{H}_{33} - \mathcal{H}_{12}^2 - \mathcal{H}_{13}^2 - \mathcal{H}_{23}^2,\\
&c = \mathrm{Det}(\mathcal{H}).
\end{aligned} \tag{C4}
$$

We take the normal ordering (NO). Therefore, we have

$$
\begin{aligned}
&m_{\nu_1} < m_{\nu_2} < m_{\nu_3}, \quad m_{\nu_1}^2 = m_1^2, \quad m_{\nu_2}^2 = m_2^2, \quad m_{\nu_3}^2 = m_3^2,\\
&\Delta m_{\odot}^2 = m_{\nu_2}^2 - m_{\nu_1}^2 = \frac{2}{\sqrt{3}}p\sin\phi > 0,\\
&\Delta m_A^2 = m_{\nu_3}^2 - m_{\nu_1}^2 = p\left(\cos\phi + \frac{1}{\sqrt{3}}\sin\phi\right) > 0.
\end{aligned} \tag{C5}
$$

From the mass squared matrix $\mathcal{H}$, the following normalized eigenvectors are obtained:

$$
\begin{aligned}
\begin{pmatrix} (U_\nu)_{11} \\ (U_\nu)_{21} \\ (U_\nu)_{31} \end{pmatrix} &= \frac{1}{\sqrt{|X_1|^2 + |Y_1|^2 + |Z_1|^2}} \begin{pmatrix} X_1 \\ Y_1 \\ Z_1 \end{pmatrix},\\
\begin{pmatrix} (U_\nu)_{12} \\ (U_\nu)_{22} \\ (U_\nu)_{32} \end{pmatrix} &= \frac{1}{\sqrt{|X_2|^2 + |Y_2|^2 + |Z_2|^2}} \begin{pmatrix} X_2 \\ Y_2 \\ Z_2 \end{pmatrix},\\
\begin{pmatrix} (U_\nu)_{13} \\ (U_\nu)_{23} \\ (U_\nu)_{33} \end{pmatrix} &= \frac{1}{\sqrt{|X_3|^2 + |Y_3|^2 + |Z_3|^2}} \begin{pmatrix} X_3 \\ Y_3 \\ Z_3 \end{pmatrix}.
\end{aligned} \tag{C6}
$$

The concrete forms of X_I, Y_I, Z_I for $I = 1,2,3$ are

$$
\begin{aligned}
X_1 &= (\mathcal{H}_{22} - m_{\nu_1}^2)(\mathcal{H}_{33} - m_{\nu_1}^2) - \mathcal{H}_{23}^2,\\
Y_1 &= \mathcal{H}_{13}\mathcal{H}_{23} - \mathcal{H}_{12}(\mathcal{H}_{33} - m_{\nu_1}^2),\\
Z_1 &= \mathcal{H}_{12}\mathcal{H}_{23} - \mathcal{H}_{13}(\mathcal{H}_{22} - m_{\nu_1}^2),\\
X_2 &= \mathcal{H}_{13}\mathcal{H}_{23} - \mathcal{H}_{12}\left(\mathcal{H}_{33} - m_{\nu_2}^2\right),
\end{aligned} \tag{C7}
$$

$$
\begin{aligned}
Y_2 &= (\mathcal{H}_{11} - m_{\nu_2}^2)(\mathcal{H}_{33} - m_{\nu_2}^2) - \mathcal{H}_{13}^2,\\
Z_2 &= \mathcal{H}_{12}\mathcal{H}_{13} - \mathcal{H}_{23}\left(\mathcal{H}_{11} - m_{\nu_2}^2\right),\\
X_3 &= \mathcal{H}_{12}\mathcal{H}_{23} - \mathcal{H}_{13}\left(\mathcal{H}_{22} - m_{\nu_3}^2\right),\\
Y_3 &= \mathcal{H}_{12}\mathcal{H}_{13} - \mathcal{H}_{23}\left(\mathcal{H}_{11} - m_{\nu_3}^2\right),\\
Z_3 &= (\mathcal{H}_{11} - m_{\nu_3}^2)(\mathcal{H}_{22} - m_{\nu_3}^2) - \mathcal{H}_{12}^2.
\end{aligned} \tag{C7}
$$

The mixing angles among three extremely small neutrinos can be defined as

$$
\begin{aligned}
\sin\theta_{13} &= \left|(U_\nu)_{13}\right|,\\
\cos\theta_{13} &= \sqrt{1 - \left|(U_\nu)_{13}\right|^2},\\
\sin\theta_{23} &= \frac{\left|(U_\nu)_{23}\right|}{\sqrt{1 - \left|(U_\nu)_{13}\right|^2}},\\
\cos\theta_{23} &= \frac{\left|(U_\nu)_{33}\right|}{\sqrt{1 - \left|(U_\nu)_{13}\right|^2}},\\
\sin\theta_{12} &= \frac{\left|(U_\nu)_{12}\right|}{\sqrt{1 - \left|(U_\nu)_{13}\right|^2}},\\
\cos\theta_{12} &= \frac{\left|(U_\nu)_{11}\right|}{\sqrt{1 - \left|(U_\nu)_{13}\right|^2}}.
\end{aligned} \tag{C8}
$$

References

[1] S. L. Glashow and H. Georgi, Phys. Rev. Lett. **32**, 438 (1974)
[2] S. Weinberg, Phys. Rev. Lett. **19**, 1264 (1967)
[3] S. Weinberg, Phys. Rev. D. **19**, 1277 (1979)
[4] A. Salam and J. C. Ward, Phys. Rev. Lett. **30**, 1268 (1973)
[5] H. P. Nilles, Phys. Rep. **110**, 1 (1984)
[6] H. E. Haber and G. L. Kane, Phys. Rept. **117**, 75 (1985)
[7] J. Rosiek, Phys. Rev. D **41**, 3464 (1990)
[8] U. Ellwanger, C. Hugonie, and A. M. Teixeira, Phys. Rep. **496**, 1 (2010)
[9] B. Yan, S. M. Zhao, and T. F. Feng, Nucl. Phys. B **975**, 115671 (2022)
[10] H. B. Zhang, T. F. Feng, Z. F. Ge *et al.*, JHEP **02**, 012 (2014)
[11] A. D. Gouvea and S. Shalgar, JCAP **04**, 018 (2013)
[12] V. Brdar, A. Greljo, J. Kopp *et al.*, JCAP **01**, 039 (2021)
[13] S. M. Zhao, T. F. Feng, M. J. Zhang *et al.*, JHEP **02**, 130 (2020)
[14] G. Belanger, J. D. Silva, and H. M. Tran, Phys. Rev. D **95**,

115017 (2017)
[15] V. Barger, P. F. Perez, and S. Spinner, Phys. Rev. Lett. **102**, 181802 (2009)
[16] P. H. Chankowski, S. Pokorski, and J. Wagner, Eur. Phys. J. C **47**, 187 (2006)
[17] J. L. Yang, T. F. Feng, S. M. Zhao *et al*., Eur. Phys. J. C **78**, 714 (2018)
[18] T. F. Feng, L. Sun, and X. Y. Yang, Nucl. Phys. B **800**, 221 (2008)
[19] R. L. Workman *et al*., Prog. Theor. Exp. Phys. **2022**, 083C01 (2022)
[20] CMS Collaboration, Phys. Lett. B **716**, 30 (2012)
[21] ATLAS Collaboration, Phys. Lett. B **716**, 1 (2012)
[22] M. Carena, J. R. Espinosa, M. Quirós *et al*., Phys. Lett. B **355**, 209 (1995)
[23] M. Carena, S. Gori, N. R. Shah *et al*., JHEP **03**, 014 (2012)
[24] F. P. An *et al*., Phys. Rev. Lett. **130**, 161802 (2023)
[25] R. Abbasi *et al*., Phys. Rev. D **108**, 012014 (2023)
[26] K. Abe *et al*., Phys. Rev. D **108**, 072011 (2023)
[27] M. Carena *et al*., Phys. Rev. D **70**, 093009 (2004)
[28] E. Aprile *et al*., Phys. Rev. Lett. **129**, 161805 (2022)
[29] S. Singirala, D. K. Singha, and R. Mohanta, Phys. Rev. D **109**, 075031 (2024)
[30] B. Dziewit, S. Zajac, and M. Zralek, Acta Phys. Pol. B **42**, 2509 (2011)